+Supporting Information (SI):

Tuning luminescence of didysprosium single-molecule magnets with π-conjugated/non-conjugated bridging ligand

Yang Liu, Bang-Heng Lyu, Shan-Nan Du, Guo-Zhang Huang, Ze-Yu Ruan, Si-Guo Wu, Jun-Liang Liu,* and Ming-Liang Tong*

[a] *Key Lab of Bioinorganic and Synthetic Chemistry of Ministry of Education, School of Chemistry, Sun Yat-Sen University, Guangzhou 510275, P. R. China*

**E-mail: liujliang5@mail.sysu.edu.cn (J.L.L.); tongml@mail.sysu.edu.cn. (M.L.T.)*;

Contents

Experimental details

All reactions and manipulations were performed under aerobic conditions. All reagents were commercially available and use without purification. The C, H, and N elemental analyses were carried out with an Elementar Vario-EL CHNS elemental analyzer. Infrared spectra (4000−400 cm^{-1}) were recorded on KBr pellets at room temperature using a Nicolet 6700-Contiumm FT/IR spectrometer. Thermogravimetric (TG) analysis was carried out on a TG-209 F3 Tarsus thermogravimetric analyzer. All magnetic measurements were performed on polycrystalline samples sealed in a polyethylene bag. AC magnetic measurements were performed at frequencies from 0.1 to 999 Hz. Magnetic susceptibility measurements were performed with a Quantum Design MPMS-3 magnetometer. Data were corrected for the diamagnetic contribution calculated from Pascal constants. Single-crystal diffraction data were collected on a Bruker D8 QUEST diffractometer with Mo K_α radiation (λ = 0.71073 Å) for complex **1** and **2** at 120 K. The data collection and reduction were carried out using the Bruker APEX3 program. The structures were solved by SHELXT methods with the Olex2 program,[1,2] and all non-hydrogen atoms were refined anisotropically by least-squares technique on weighted F^2 values using SHELXL.[3] Anisotropic thermal parameters were assigned to all non-hydrogen atoms. The hydrogen atoms attached to C and N atoms were placed in idealized positions and refined using a riding model to the atom to which they were attached. X-ray powder diffraction intensities for polycrystalline samples sealed in the capillaries were measured on SmartLab X-ray Diffractometer (Cu-K_α, λ = 1.54056 Å) at 120 K. The luminescence spectra were recorded on an Edinburgh FLS-980 Fluorescence spectrometer equipped with Xenon light, PMT detector, and ALS cryostat.

Synthesis of [Dy$_2$(bbpen)$_2$(tpb)(MeOH)$_2$](BPh$_4$)$_2$·2MeOH (**1**) [Dy(bbpen)NO$_3$] and tpb were prepared according to the literatures.[4–8] A mixture of [Dy(bbpen)NO$_3$] (0.034 g, 0.05 mmol) and tpb (0.010 g, 0.025 mmol) in 10 mL MeOH was stirred at 50 °C until the solid was dissolved completely. After that, NaBPh$_4$ (0.017 g, 0.05 mmol) was added to the resulting mixture. Then the mixture was immediately filtered and stand at room temperature. After few days, colourless block crystals were obtained in *ca*. 32% yield. Anal. calcd (%) for $C_{134}H_{130}B_2Dy_2N_{12}O_8$: C 67.53, H 5.50, N 7.05. Found (%): C 67.25, H 5.45, N 7.04. IR (cm^{-1}) for **1**: 3562 (br), 3053 (vs), 3001 (w), 2933 (s), 2883 (w), 2846 (s), 2578 (br), 1940 (w), 1882 (w), 1813 (w), 1772 (w), 1710 (w), 1601 (vs), 1481 (vs), 1446 (vs), 1381 (m), 1300 (vs).

Synthesis of [Dy$_2$(bbpen)$_2$(tpcb)(MeOH)$_2$](BPh$_4$)$_2$ (**2**) [Dy(bbpen)NO$_3$] and tpcb were prepared according to the literatures.[4–7,9] A mixture of [Dy(bbpen)NO$_3$] (0.014 g, 0.02 mmol) and tpcb (0.0036 g, 0.01 mmol) in 10 mL MeOH was stirred at 50 °C until the solid was dissolved completely. After that, NaBPh$_4$ (0.0068 g, 0.02 mmol) was added to the resulting mixture. Then the mixture was immediately filtered and stand at room temperature. After few days, colourless block crystals were obtained in *ca*. 30% yield. Anal. calcd (%) for $C_{130}H_{124}B_2Dy_2N_{12}O_6$: C 67.97, H 5.44, N 7.32. Found (%): C 67.75, H 5.23, N 7.14. IR (cm^{-1}) for **2**: 3424 (br), 3053 (vs), 3000 (w), 2943 (s), 2883 (w), 2844 (s), 2609 (w), 1940 (w), 1882 (w), 1817 (w), 1772 (w), 1601 (vs), 1481 (vs), 1452 (vs), 1375 (m), 1298 (vs).

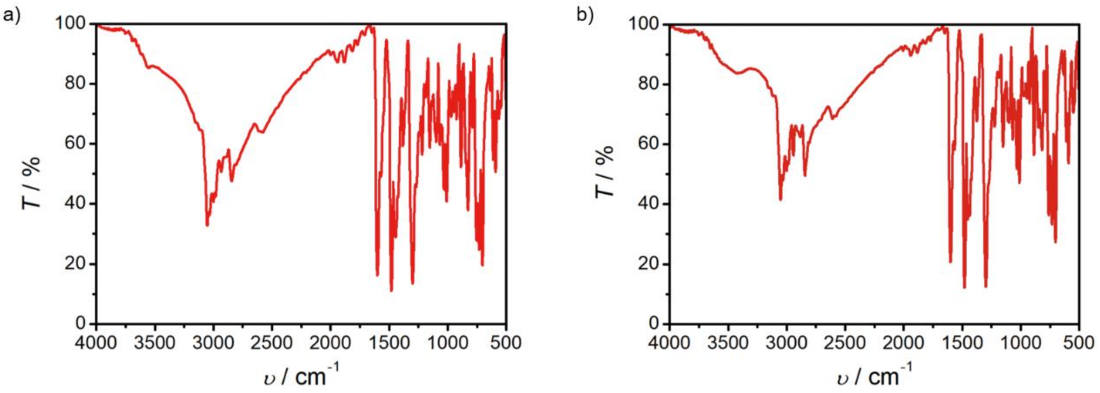

Fig. S1. Infrared spectra for **1** (a) and **2** (b).

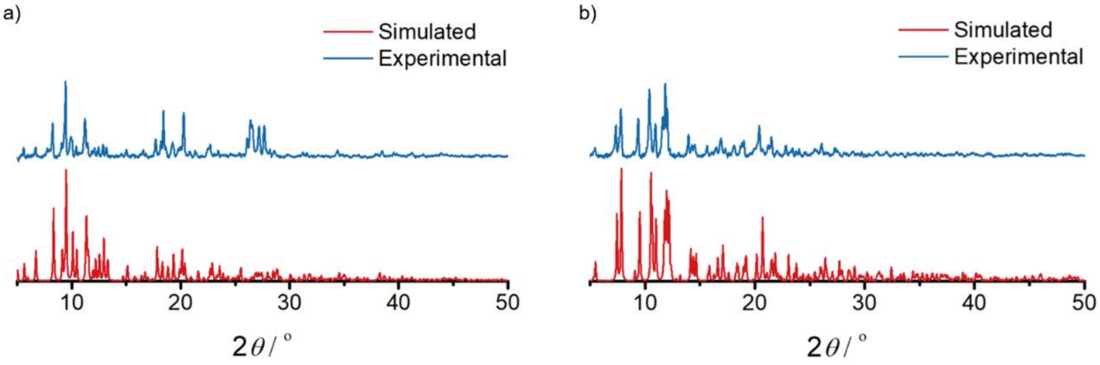

Fig. S2. Experimental and simulated X-ray powder diffraction patterns for **1** (a) and **2** (b).

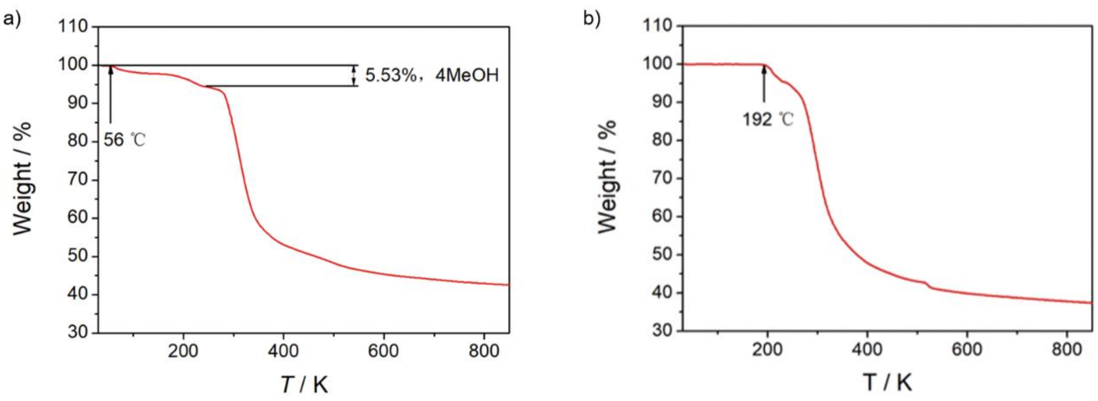

Fig. S3. Thermogravimetric analysis for **1** (a) and **2** (b) under N_2 atmosphere.

Luminescent characterization We performed luminescence measurements on polycrystalline samples around 6 K. The excitation spectra of **2** exhibits characteristic peaks from Dy(III) (Fig S6), whereas that of **1** only shows photoluminescence of tpb (Fig S4a). This result confirms again that the energy transfer is reduced in **1** due to the conjugation effect of tpb.

As shown in Fig. S4b and S5, **1** was irradiated at 300 and 383.5 nm, respectively. None of these emission spectra and that irradiated at 322.7 nm show strong lanthanide luminescence. So we chose 322.7 nm as the excitation wavelength in order to better compare with **2** under the same instrument parameters (Fig. 3). As revealed in Fig S8, the emission spectra of both ligands show broad and strong peaks, and there are no peaks as sharp as those from lanthanide ions.

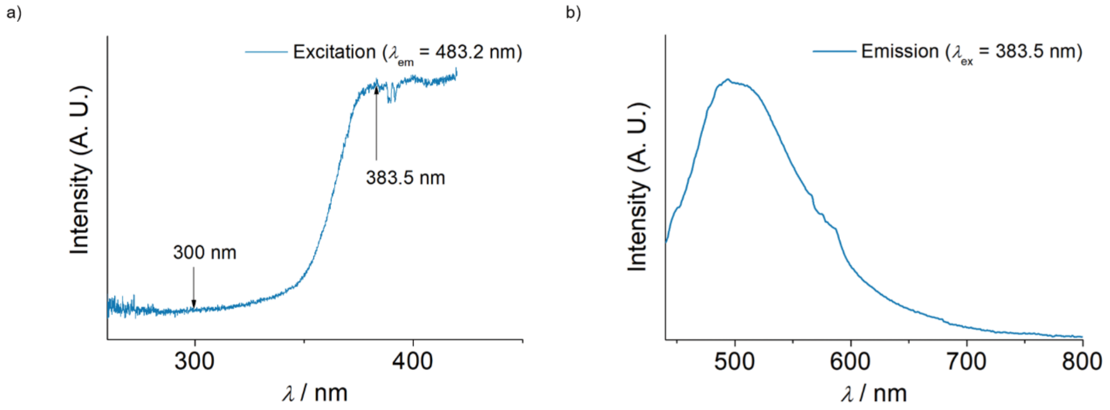

Fig. S4. The plots of excitation spectrum (a) and emission spectrum (b) for **1** around 6 K.

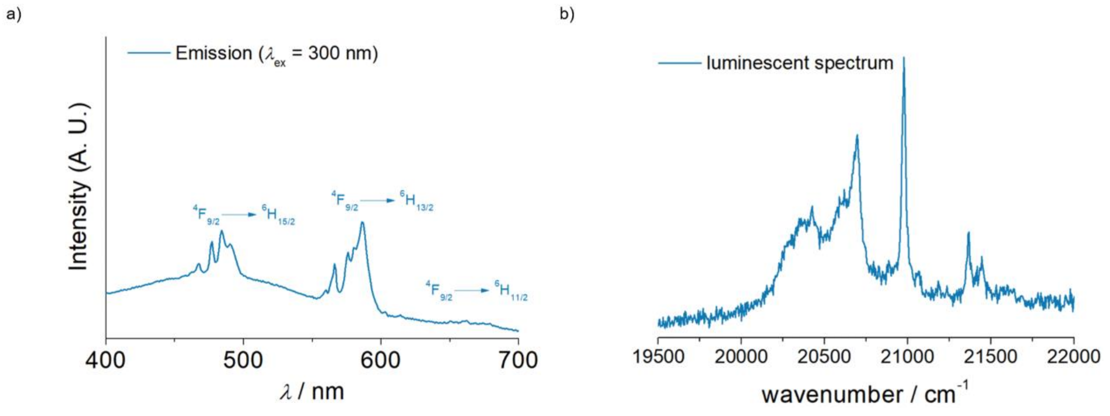

Fig. S5. The plots of emission spectrum (a) and the enlarged view on $^4F_{9/2}\rightarrow{}^6H_{15/2}$ transition (b) for **1** around 6 K.

Table S1 Energy peak center (Energy, cm^{-1}) and full-width-at-half-maximum (FWHM, cm^{-1}) of the $^4F_{9/2}\rightarrow{}^6H_{15/2}$ of **2** calculating from simulation of the experimental emission spectrum excited at 322.7 nm at 6 K using Lorentz function fit.

Energy (cm^{-1})	20279.2	20404.0	20457.8	20561.8	20601.2	20667.7	20974.1	213722.5
FWHM (cm^{-1})	39.8	45.8	38.4	21.5	14.4	24.3	13.3	15.2

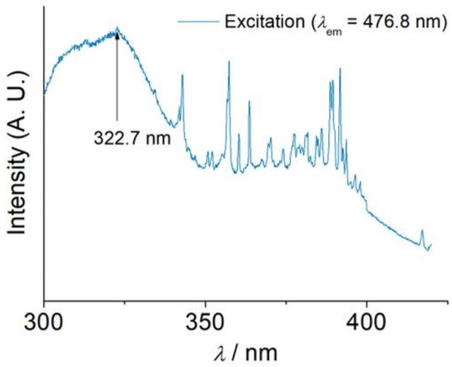

Fig. S6. The plots of excitation spectrum for **2** at around 6 K.

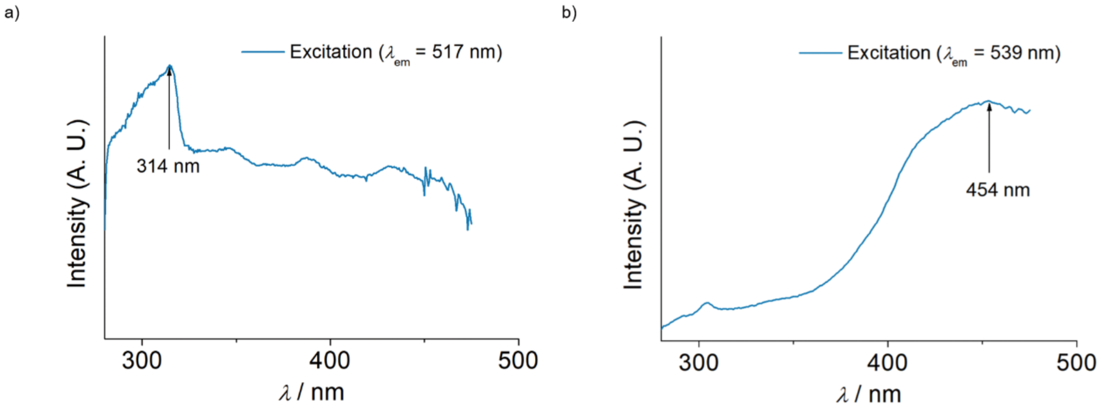

Fig. S7. The plots of excitation spectrum for tpb (a) and tpcb (b) ligand at around 6 K.

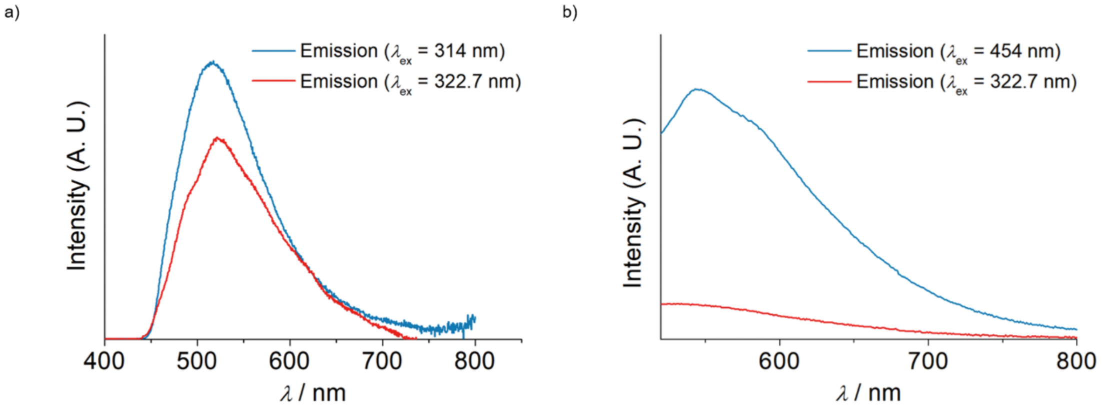

Fig. S8. The plots of emission spectrum for tpb (a) and tpcb (b) ligand at around 6 K.

Table S2. Crystal data and structure refinement parameters for **1** and **2**.

Complex	**1**	**2**
Empirical formula	$C_{134}H_{130}B_2Dy_2N_{12}O_8$	$C_{130}H_{124}B_2Dy_2N_{12}O_6$
Formula weight	2383.11	2297.02
Temperature / K	120	120
Crystal system	Triclinc	Monoclinic
Space group	*P*−1	*C*2/*c*
a / Å	16.4469(8)	33.2765(11)
b / Å	18.6601(11)	10.1813(3)
c / Å	20.4290(12)	32.2152(11)
α / °	73.848(2)	90
β / °	76.884(2)	93.1020(10)
γ / °	74.783(2)	90
V / Å^3	5730.4(6)	10898.5(6)
Z	2	4
ρ_{calc} / g cm^{-3}	1.372	1.400
F(000)	2430.0	4712.0
μ (mm^{-1})	1.358	1.425
Goodness-of-fit on F^2	1.014	1.122
R_1, wR_2 [$I \geq 2\sigma(I)$]^a	0.0350, 0.0605	0.0300, 0.0542
R_1, wR_2 [all data]^b	0.0687, 0.0688	0.0427, 0.0573
Largest diff. peak/hole / e Å^{-3}	0.69/-0.77	0.74/-0.63

^{a} $R_1 = \sum||F_o| - |F_c||/\sum|F_o|$. $wR_2 = [\sum w(F_o^2 - F_c^2)^2/\sum w(F_o^2)$

Table S3. The CShM values calculated by SHAPE 2.1[10,11] for Dy(III) ion in **1** and **2**.

	OP-8 (D_{8h})	**HPY-8 (C_{7v})**	**HBPY-8 (D_{6h})**	**CU-8 (O_h)**	**SAPR-8 (D_{4d})**	**TDD-8 (D_{2d})**	**JGBF-8 (D_{2d})**
1_{Dy1}	33.180	21.305	10.173	6.123	*2.348*	3.049	11.223
1_{Dy2}	32.836	21.398	11.169	6.947	*2.040*	2.214	11.639
2_{Dy}	32.996	21.572	11.369	8.281	2.487	*2.198*	10.705

	JETBPY-8 (D_{3h})	**JBTP-8 (C_{2v})**	**BTPR-8 (C_{2v})**	**JSD-8 (D_{2d})**	**TT-8 (T_d)**	**ETBPY-8 (D_{3h})**
1_{Dy1}	26.222	3.857	3.572	5.539	6.929	22.540
1_{Dy2}	26.879	2.992	2.948	5.280	7.725	22.808
2_{Dy}	26.886	2.584	2.732	4.600	8.976	22.824

OP-8 = Octagon; HPY-8 = Heptagonal pyramid; HBPY-8 = Hexagonal bipyramid; CU-8 = Cube; SAPR-8 = Square antiprism; TDD-8 = Triangular dodecahedron; JGBF-8 = Johnson-Gyrobifastigium (J26); JETBPY-8 = Johnson - Elongated triangular bipyramid (J14); JBTP-8 = Johnson-Biaugmented trigonal prism (J50); BTPR-8 = Biaugmented trigonal prism; JSD-8 = Snub disphenoid (J84); TT-8 = Triakis tetrahedron; ETBPY-8 = Elongated trigonal bipyramid

Table S4. Selected bond lengths (Å) and angles (°) for complex **1** and **2**.

bond	**1**	**2**	**bond angle**	**1**	**2**
Dy1–O1	2.203(2)	2.1890(16)	O1−Dy1−O3	83.15(8)	81.87(6)
Dy1–O2	2.196(2)	2.1713(16)	O1−Dy1−N1	106.96(8)	72.29(6)
Dy1–O3	2.433(2)	2.4110(16)	O1−Dy1−N2	74.30(8)	82.55(6)
Dy1–N1	2.580(3)	2.6550(18)	O1−Dy1−N3	127.20(8)	126.27(6)
Dy1–N2	2.638(3)	2.5431(19)	O1−Dy1−N4	81.37(8)	109.34(6)
Dy1–N3	2.631(2)	2.6247(18)	O1−Dy1−N5	77.90(8)	77.69(6)
Dy1–N4	2.548(3)	2.5655(19)	O2−Dy1−O1	157.97(8)	155.93(6)
Dy1–N5	2.550(3)	2.5879(19)	O2−Dy1−O3	79.73(8)	84.39(6)
Dy2–O4	2.214(3)		O2−Dy1−N1	77.67(9)	131.44(6)
Dy2–O5	2.175(2)		O2−Dy1−N2	125.27(8)	97.98(6)
Dy2–O6	2.403(3)		O2−Dy1−N3	73.36(8)	73.79(6)
Dy2–N8	2.542(3)		O2−Dy1−N4	105.56(9)	83.72(6)
Dy2–N9	2.538(3)		O2−Dy1−N5	83.45(8)	79.26(6)
Dy2–N10	2.636(3)		O3−Dy1−N1	138.03(8)	111.31(6)
Dy2–N11	2.598(3)		O3−Dy1−N2	153.58(9)	145.16(6)
Dy2–N12	2.553(3)		O3−Dy1−N3	115.94(8)	147.26(6)
			O3−Dy1−N4	70.53(8)	68.96(6)
			O3−Dy1−N5	70.96(8)	71.60(6)
			N2−Dy1−N1	63.84(8)	93.14(6)
			N2−Dy1−N3	69.90(8)	63.82(6)
			N2−Dy1−N4	92.28(8)	145.86(6)
			N2−Dy1−N5	116.21(8)	74.73(6)
			N3−Dy1−N1	90.62(8)	69.36(6)
			N4−Dy1−N1	150.07(9)	62.52(6)
			N4−Dy1−N3	63.01(8)	84.37(6)
			N4−Dy1−N5	137.94(8)	138.22(6)
			N5–Dy1–N1	71.68(8)	148.86(6)
			N5−Dy1−N3	153.50(8)	125.73(6)
			O4−Dy2−O6	79.80(9)	
			O4−Dy2−N8	80.07(8)	
			O4−Dy2−N9	111.16(9)	
			O4−Dy2−N10	74.29(8)	
			O4−Dy2−N11	127.41(8)	
			O4−Dy2−N12	79.78(9)	
			O5−Dy2−O4	155.37(8)	
			O5−Dy2−O6	83.84(9)	
			O5−Dy2−N8	77.46(9)	
			O5−Dy2−N9	80.30(9)	
			O5−Dy2−N10	129.55(8)	
			O5−Dy2−N11	73.26(8)	
			O5−Dy2−N12	102.25(9)	
			O6−Dy2−N8	72.26(9)	

O6−Dy2−N9	71.16(9)
O6−Dy2−N10	113.08(9)
O6−Dy2−N11	150.69(9)
O6−Dy2−N12	140.73(9)
N8−Dy2−N10	152.05(9)
N8−Dy2−N11	118.59(8)
N8−Dy2−N12	71.41(9)
N9−Dy2−N8	138.74(9)
N9−Dy2−N10	63.42(8)
N9−Dy2−N11	86.86(9)
N9−Dy2−N12	147.98(9)
N11−Dy2−N10	71.05(8)
N12–Dy2–N10	92.97(8)
N12−Dy2−N11	64.09(9)

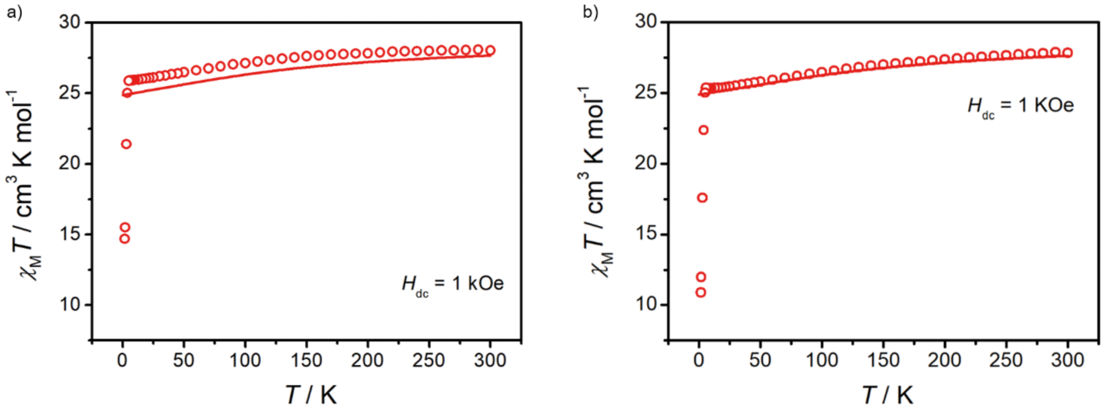

Fig. S9. Temperature-dependent molar magnetic susceptibility for **1** (a) and **2** (b) from 2 to 300 K under a 1 kOe direct-current field. The line corresponds to the *ab initio* calculations.

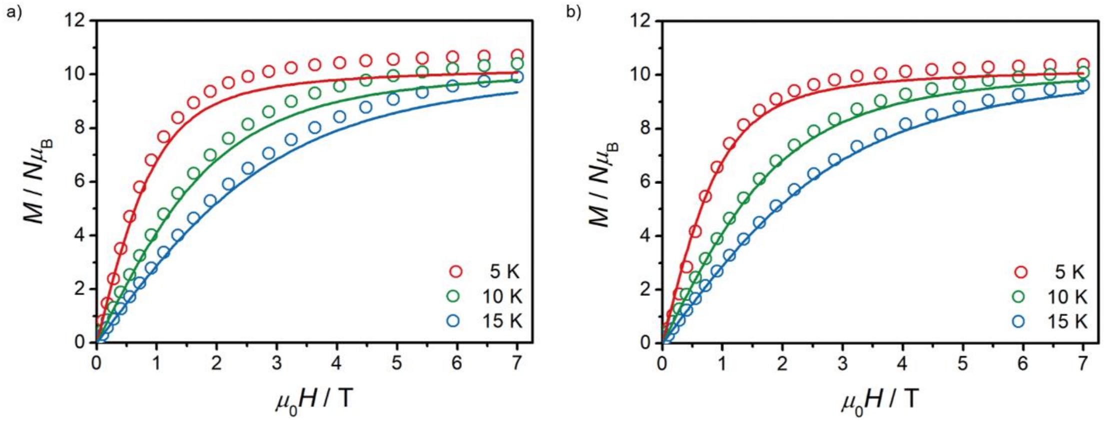

Fig. S10. Variable-temperature field-dependent magnetization data for **1** (a) and **2** (b). Data were collected from 0 to 7 T in steady fields. The solid lines correspond to the results from *ab initio* calculations.

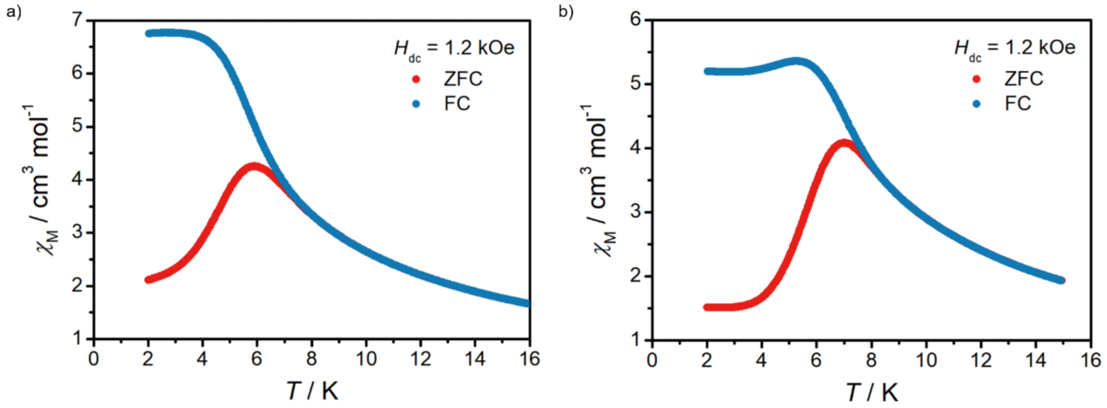

Fig. S11. The plot of ZFC/FC magnetic susceptibilities under 1.2 kOe, which diverges at 7 K for **1** (a) and 8 K for **2** (b). We take the normalized difference of ZFC and FC magnetization of 1% as a cut-off criterion.[12]

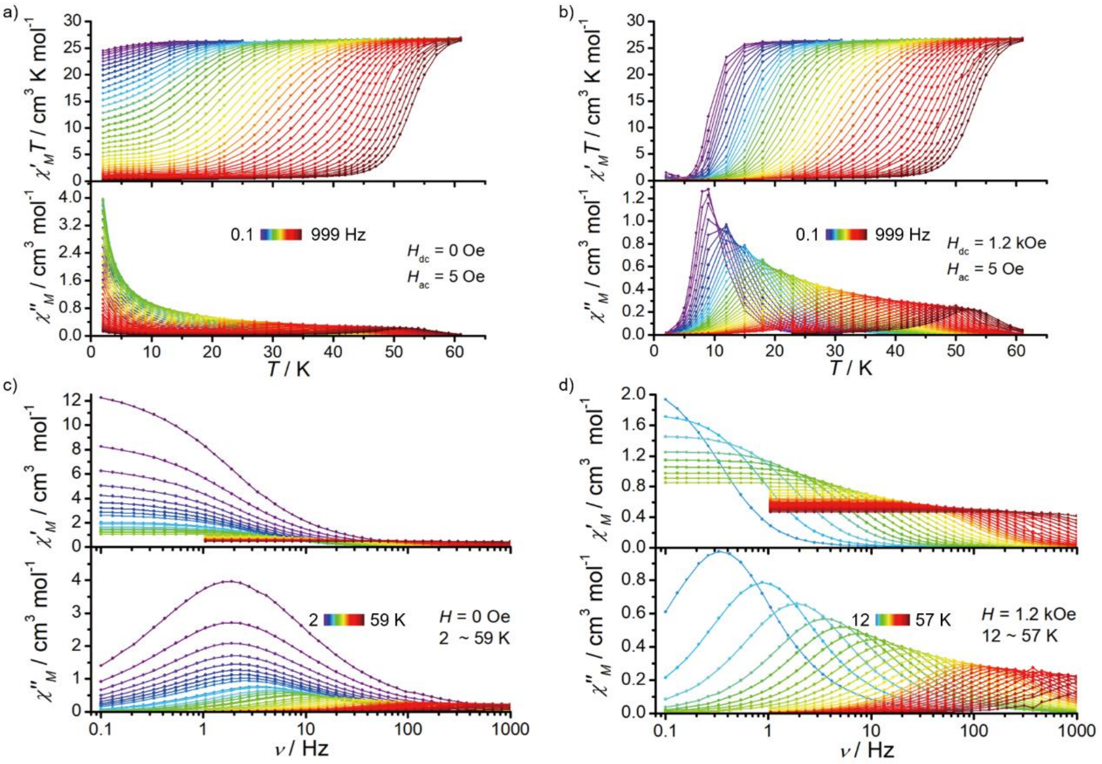

Fig. S12 Variable-temperature (top) and variable-frequency (bottom) ac magnetic susceptibilities for **1** under 0 Oe and 1.2 kOe. The solid lines are guided for the eyes.

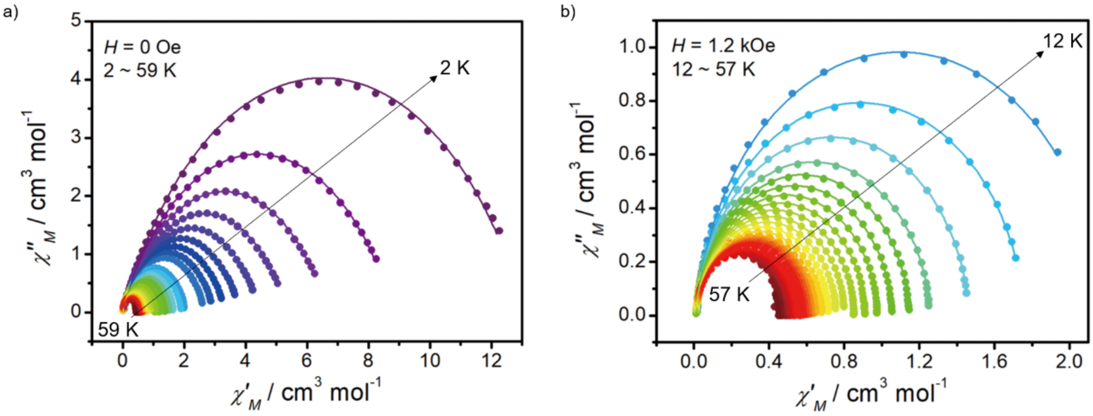

Fig. S13. Cole-Cole plots for **1** under 0 Oe (α = 0-0.30) for 2-59 K and 1.2 kOe (α = 0.029-0.063) for 12-57 K. The solid lines are best fit for the generalized Debye model.

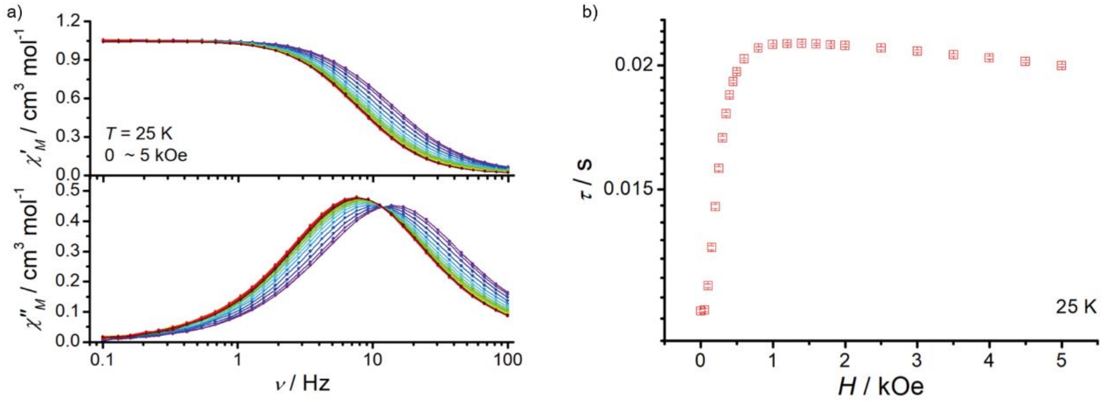

Fig. S14. Variable-field ac magnetic susceptibilities for **1** (a) and field-dependence of magnetic relaxation times (τ) for **1** at 25 K. The solid lines are guided for the eyes.

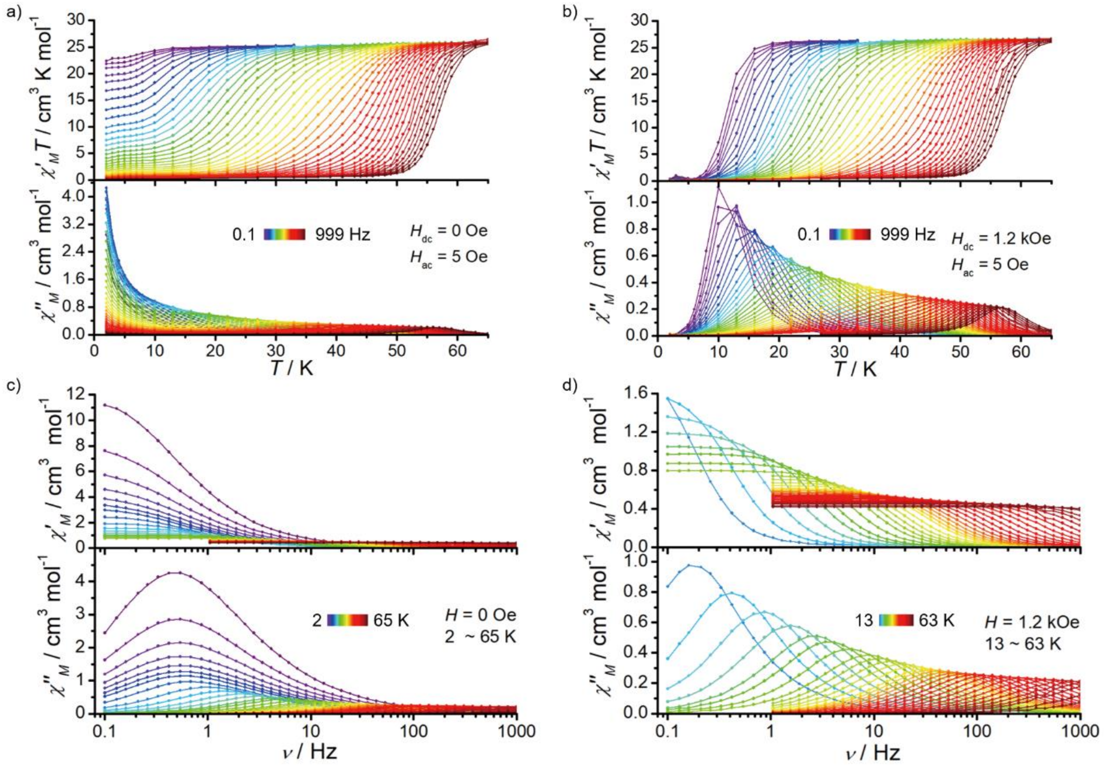

Fig. S15 Variable-temperature (top) and variable-frequency (bottom) ac magnetic susceptibilities for **2** under 0 Oe and 1.2 kOe. The solid lines are guided for the eyes.

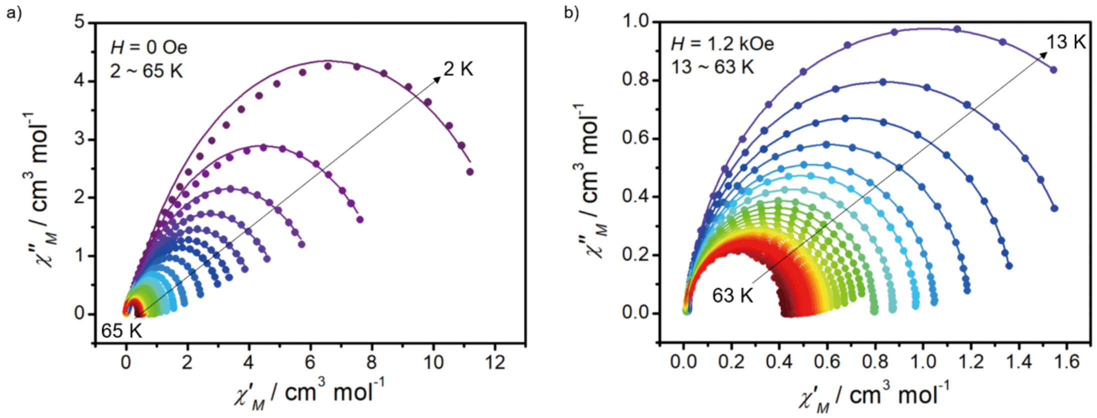

Fig. S16. Cole-Cole plots for **2** under 0 Oe (α = 0-0.27) for 2-65 K and 1.2 kOe (α = 0-0.040) for 13-63 K. The solid lines are best fit for the generalized Debye model.

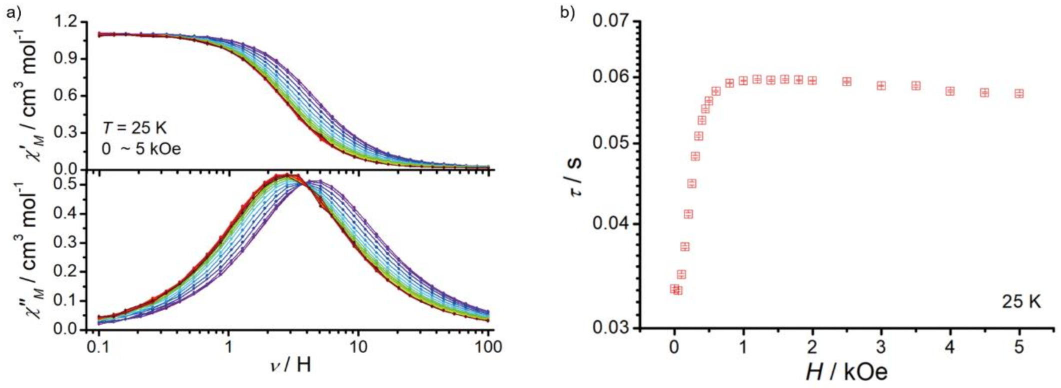

Fig. S17. Variable-field ac magnetic susceptibilities for **2** (a) and field-dependence of magnetic relaxation times (τ) for **2** at 25 K. The solid lines are guided for the eyes.

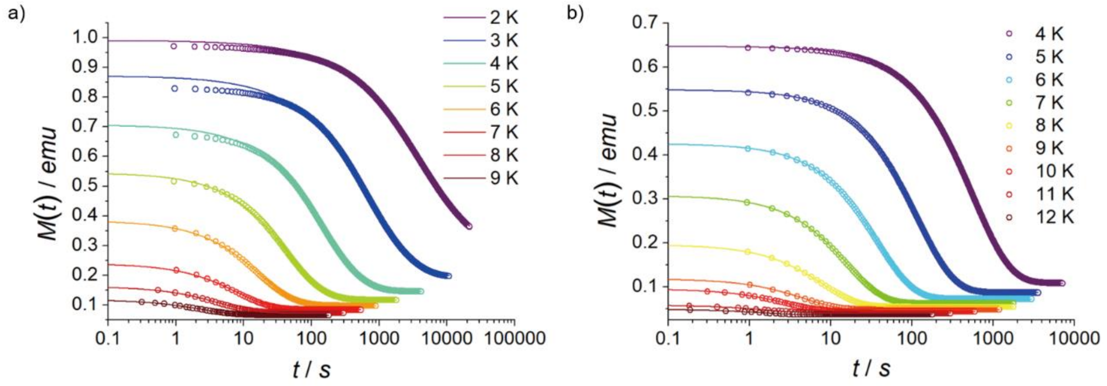

Fig. S18. The plots of dc magnetization decay for **1** (a) and **2** (b) with final field of 1.2 kOe. The magnetic field was ramped to 2 T and the temperature was declined to the indicated temperature. After temperature and magnetic moment are steady, the magnetic field decreases to 1.2 kOe, and kept unchanged for at least 10^3 ~ 10^4 s depending on the measured temperature, whilst magnetization was measured. The solid lines are the best fit to the exponential decay as $M(t) = M_f + (M_i - M_f)\exp[-(t/\tau)^{\beta}]$, where τ is the relaxation time.

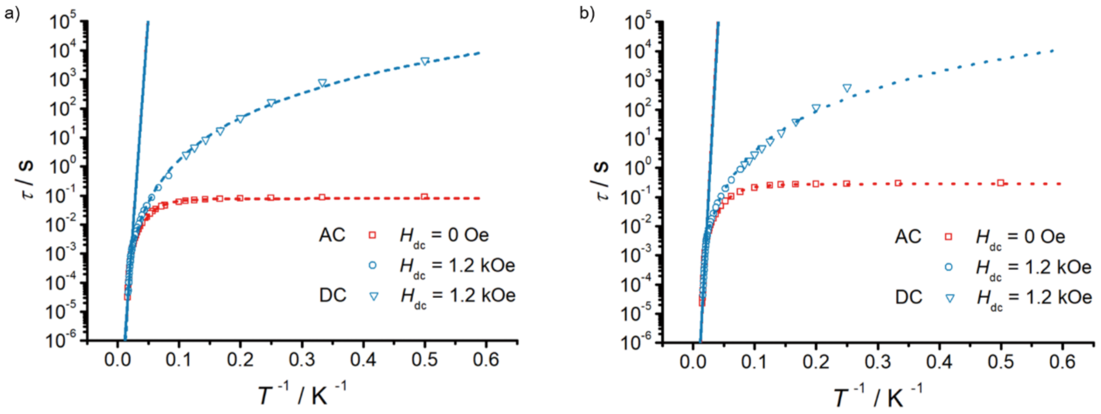

Fig. S19. The variable temperature relaxation time τ versus T^{-1} plot under 0 Oe (red) and 1.2 kOe (blue) for **1** (a) and **2** (b). The solid lines corresponding to Arrhenius law at high temperature. The dashed lines are from the best fits of $\tau = \tau_0^{-1}\exp(-U_{eff}/k_BT) + CT^n + \tau_{QTM}^{-1}$. For complex **1**, obtaining the parameters U_{eff}/k_B = 780(22) K, τ_0 = 8(3) × 10^{-11} s, C = 6(1) × 10^{-4} s^{-}1 K^{-n}, n = 3.67(7) and τ_{QTM} = 0.078(2) s under 0 Oe, and U_{eff}/k_B = 939(77) K, τ_0 = 5(7) × 10^{-12} s, C = 8.8(8) × 10^{-6} s^{-1} K^{-n} and n = 4.83(3) under 1.2 kOe. For complex **2**, obtaining the parameters U_{eff}/k_B = 967(10) K, τ_0 = 8(1) × 10^{-12} s, C = 2.7(4) × 10^{-4} s^{-1} K^{-n}, n = 3.59(4) and τ_{QTM} = 0.280(4) s under 0 Oe, and U_{eff}/k_B = 1006(66) K, τ_0 = 5(5) × 10^{-12} s, C = 8(1) × 10^{-6} s^{-1} K^{-n} and n = 4.54(6) under 1.2 kOe. In theory, the Raman exponent (n) is 9 for Kramers ions based on some approximations. In fact, n around 4 is practically reasonable due to the divergence between phonon spectrum and Debye model,[13–15] which is common observed in other SMMs.[16–18]

Computational details All *ab initio* calculations were carried out with OpenMOLCAS version 18.09[19] and are of the CASSCF/RASSI type. The Cholesky decomposition threshold was set to 1 × 10^{-8} to save disk space. An entire molecule was included, and the coordinates of atoms were extracted from the experimentally determined crystal structure. The neighbouring Dy(III) site was computationally replaced by the diamagnetic Lu(III) ANO-RCC basis set approximations have been employed (see Table S5)[20–22]. Active space of the CASSCF method included nine electrons in seven 4f orbitals of Dy(III). 21 sextets for Dy(III) were optimized in state-averaged calculations and then mixed by spin−orbit coupling using RASSI approach.[23] The *g*-tensors, energies, main magnetic axis as well as the magnetizations were obtained by SINGLE_ANISO routine.[24]

Table S5. The employed ANO-RCC basis sets for complexes **1** and **2**.

1	**2**
Dy.ANO-RCC-VTZP	Dy.ANO-RCC-VTZP
Y.ANO-RCC-VDZP	Y.ANO-RCC-VDZP
O.ANO-RCC-VDZP	O.ANO-RCC-VDZP
N.ANO-RCC-VDZP	N.ANO-RCC-VDZP
C.ANO-RCC-VDZ	C.ANO-RCC-VDZ
H.ANO-RCC-MB	H.ANO-RCC-MB

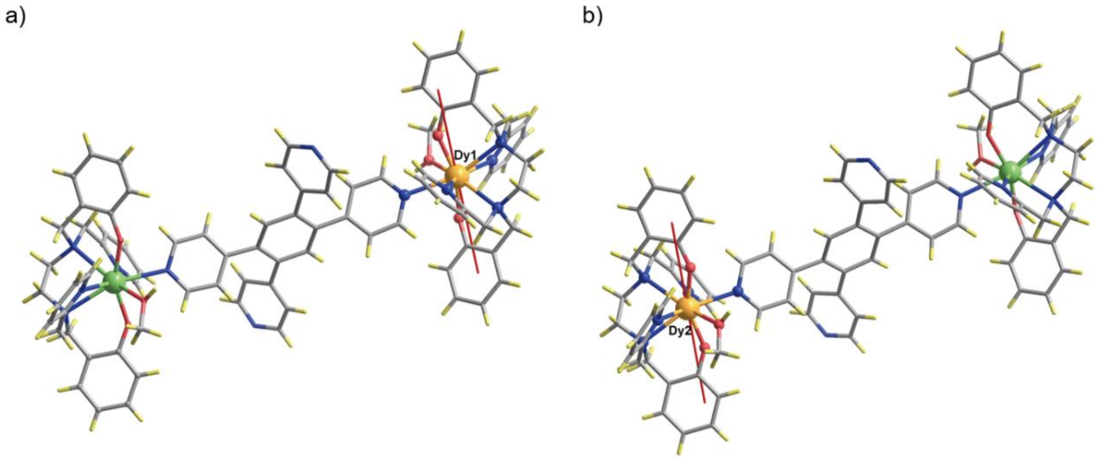

Fig S20. Molecular structure for **1** with the orientation of the main magnetic axis of the ground Kramers doublet (red line). Color code: Dy, orange; Y, green; O, red; N, blue; C, gray; H, yellow.

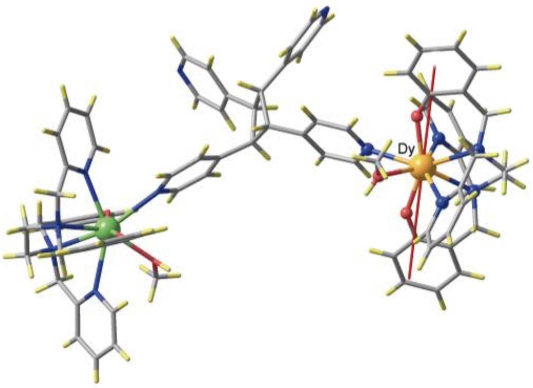

Fig S21. Molecular structure for **2** with the orientation of the main magnetic axis of the ground Kramers doublet (red line). Color code: Dy, orange; Y, green; O, red; N, blue; C, gray; H, yellow.

Table S6. Energies (K), *g*-tensors (g_X, g_Y, g_Z) and angles (°) between the main magnetic axes of the lowest Kramers doublets for the local Dy(III) sites of complexes **1** and **2**.

KD	$\mathbf{1}_{\mathbf{Dy1}}$			$\mathbf{1}_{\mathbf{Dy2}}$			**2**		
	E	***g***	***angle***	***E***	***g***	***angle***	***E***	***g***	**angle**
1	0	0.0006 0.0006 19.948	0	0	0.0002 0.0003 19.944	0	0	0.0002 0.0002 19.950	0
2	487.52	0.0463 0.0515 17.031	2.6205	474.19	0.0314 0.0327 17.054	3.7101	512.78	0.0149 0.0159 17.057	3.5793
3	935.65	0.3131 0.4699 13.782	3.7980	911.80	0.1340 0.2021 13.927	5.5320	970.07	0.1672 0.2140 13.995	5.1418
4	1185.93	2.9638 3.3255 13.609	80.518	1171.99	0.0855 1.5316 12.556	75.579	1238.15	1.6381 4.1691 12.119	81.620
5	1245.57	0.6625 3.6046 12.210	84.886	1214.70	0.0264 2.4432 10.268	63.740	1269.07	2.0046 5.3842 9.8235	78.946
6	1337.42	0.6234 4.1461 11.779	77.452	1270.04	10.475 7.7153 2.0123	71.411	1344.74	1.2144 4.9788 12.136	66.883
7	1417.10	0.7707 1.9569 17.046	78.150	1388.06	0.4961 1.0137 17.842	69.400	1418.69	0.6521 1.4306 16.356	65.281
8	1564.42	0.2611 0.6573 18.825	66.174	1547.67	0.0982 0.3803 19.274	66.005	1539.78	0.0474 0.4566 18.925	65.615

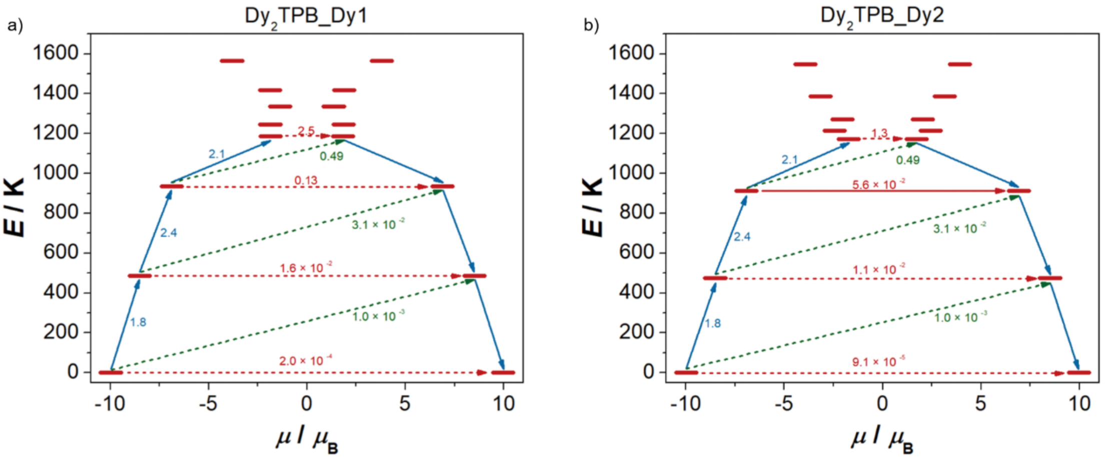

Fig. S22. Magnetization blocking barriers for **1**. The lowest 16 spin-orbit states are arranged according to the energy levels and their magnetic moments. The numbers next to arrows connecting two states display the average transition magnetic moment matrix element between the corresponding states.

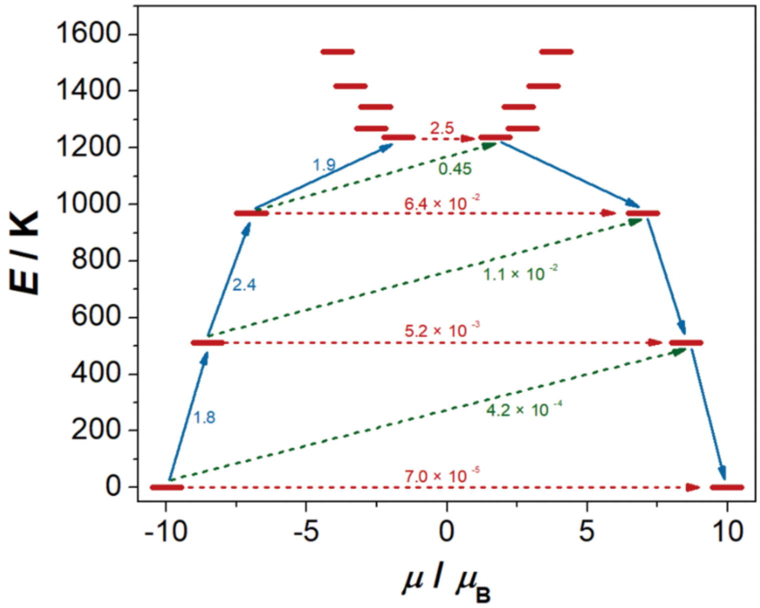

Fig. S23. Magnetization blocking barriers for **2**. The lowest 16 spin-orbit states are arranged according to the energy levels and their magnetic moments. The numbers next to arrows connecting two states display the average transition magnetic moment matrix element between the corresponding states.

References

1. G. Sheldrick, *Acta Crystallographica Section A*, 2015, **71**, 3-8.
2. O. V. Dolomanov, L. J. Bourhis, R. J. Gildea, J. A. K. Howard and H. Puschmann, *J. Appl. Crystallogr.*, 2009, **42**, 339-341.
3. G. Sheldrick, *Acta Crystallogr., Sect. C: Struct. Chem.*, 2015, **71**, 3-8.
4. T. Gregorio, A. L. Rudiger, G. G. Nunes, J. F. Soares and D. L. Hughes, *Acta Crystallogr. E*, 2015, **71**, 65-68.
5. I. A. Setyawati, S. Liu, S. J. Rettig and C. Orvig, *Inorg. Chem.*, 2000, **39**, 496-507.
6. Y. Yamada, S.-I. Takenouchi, Y. Miyoshi and K.-I. Okamoto, *J. Coord. Chem.*, 2010, **63**, 996-1012.
7. Y. Liu, Y.-C. Chen, J. Liu, W.-B. Chen, G.-Z. Huang, S.-G. Wu, J. Wang, J.-L. Liu and M.-L. Tong, *Inorg. Chem.*, 2020, **59**, 687-694.
8. Y.-C. Chang and S.-L. Wang, *J. Am. Chem. Soc.*, 2012, **134**, 9848-9851.
9. L. R. MacGillivray, J. L. Reid and J. A. Ripmeester, *J. Am. Chem. Soc.*, 2000, **122**, 7817-7818.
10. D. Casanova, M. Llunell, P. Alemany and S. Alvarez, *Chem. – Eur. J.*, 2005, **11**, 1479-1494.
11. S. Alvarez, P. Alemany, D. Casanova, J. Cirera, M. Llunell and D. Avnir, *Coord. Chem. Rev.*, 2005, **249**, 1693-1708.
12. J.-L. Liu, Y.-C. Chen and M.-L. Tong, *Chem. Soc. Rev.*, 2018, **47**, 2431-2453.
13. K. N. Shrivastava, *Phys. Status Solidi B*, 1972, **51**, 377-387.
14. K. N. Shrivastava, *Phys. Status Solidi B*, 1983, **117**, 437-458.
15. A. Singh and K. N. Shrivastava, *Phys. Status Solidi B*, 1979, **95**, 273-277.
16. S.-G. Wu, Y.-Y. Peng, Y.-C. Chen, J.-L. Liu and M.-L. Tong, *Dalton Trans.*, 2020, **49**, 14140-14147.
17. M. Perfetti, M. Gysler, Y. Rechkemmer-Patalen, P. Zhang, H. Taştan, F. Fischer, J. Netz, W. Frey, L. W. Zimmermann, T. Schleid, M. Hakl, M. Orlita, L. Ungur, L. Chibotaru, T. Brock-Nannestad, S. Piligkos and J. van Slageren, *Chem. Sci.*, 2019, **10**, 2101-2110.
18. Y. Liu, Y.-C. Chen, J. Liu, W.-B. Chen, G.-Z. Huang, S.-G. Wu, J. Wang, J.-L. Liu and M.-L. Tong, *Inorg. Chem.*, 2020, **59**, 687-694.
19. F. Aquilante, J. Autschbach, R. K. Carlson, L. F. Chibotaru, M. G. Delcey, L. De Vico, I. Fdez. Galván, N. Ferré, L. M. Frutos, L. Gagliardi, M. Garavelli, A. Giussani, C. E. Hoyer, G. Li Manni, H. Lischka, D. Ma, P. Å. Malmqvist, T. Müller, A. Nenov, M. Olivucci, T. B. Pedersen, D. Peng, F. Plasser, B. Pritchard, M. Reiher, I. Rivalta, I. Schapiro, J. Segarra-Martí, M. Stenrup, D. G. Truhlar, L. Ungur, A. Valentini, S. Vancoillie, V. Veryazov, V. P. Vysotskiy, O. Weingart, F. Zapata and R. Lindh, *J. Comput. Chem.*, 2016, **37**, 506-541.
20. B. O. Roos, R. Lindh, P.-Å. Malmqvist, V. Veryazov, P.-O. Widmark and A. C. Borin, *J. Phys. Chem. A*, 2008, **112**, 11431-11435.
21. B. O. Roos, R. Lindh, P.-Å. Malmqvist, V. Veryazov and P.-O. Widmark, *J. Phys. Chem. A*, 2004, **108**, 2851-2858.
22. B. O. Roos, R. Lindh, P.-Å. Malmqvist, V. Veryazov and P.-O. Widmark, *J. Phys. Chem. A*, 2005, **109**, 6575-6579.
23. P. Å. Malmqvist, B. O. Roos and B. Schimmelpfennig, *Chem. Phys. Lett.*, 2002, **357**,

230-240.
24. L. F. Chibotaru and L. Ungur, *J. Chem. Phys.*, 2012, **137**, 064112.